AMERICAN JOURNAL OF MATERIALS AND NANOTECHNOLOGY

The Interface Microstructures and Mechanical Properties of Laser Additive Repaired Inconel 625 Alloy

Yiyun Wei, Guomin Le, Qingdong Xu *, Lei Yang, Ruiwen Li and Wenyuan Wang

Institute of Materials, China Academy of Engineering Physics, Mianyang 621908, China;

Abstract: The microstructure and micro-mechanics around the repaired interface, and the tensile properties of laser additive repaired (LARed) Inconel 625 alloy were investigated. The results showed that the microstructure around the repaired interface was divided into three zones: the substrate zone (SZ), the heat-a ected zone (HAZ), and the repaired zone (RZ). The microstructure of the SZ had a typical equiaxed crystal structure, displaying simultaneously precipitated block-shaped MC-type carbides (NbC, TiC), with bimodal sizes of approximately 10 m and 0.5 m and an irregularly shaped flocculent Laves phase. Recrystallization occurred in the HAZ, and led to significant grain growth; a portion of the second phase dissolved in the original grain boundaries. In the RZ, there was a columnar crystal structure, and the size increased with increasing deposition thickness. Moreover, the microstructure between the layer interface and layer interior was quite di erent, presenting an overlapping transition zone (OTZ), in which the dendritic structure coarsened and more Laves phase were precipitated, compared to in the layer interior. The hardness and tensile properties of the LARed samples were equivalent to those of the wrought substrate, which indicates that laser additive repairing (LAR) is a reliable repair solution for damaged and mis-machined components comprising Inconel 625 alloy.

Keywords: laser additive repairing; Inconel 625 alloy; interface microstructures; micro-mechanics

1. Introduction

Inconel 625 is a nickel–chromium solid-solution strengthened alloy, which is largely strengthened by Nb and Mo [1,2]. It is widely used to fabricate high-temperature components in aeronautical, aerospace, marine, chemical, and nuclear industries, due to its extraordinary combination of high yield and tensile strength, excellent creep strength, and outstanding corrosion resistance at elevated temperature [3–5]. However, these components are easily damaged owing to their aggressive service conditions, and can also be mis-machined during processing [6]. If these damaged and mis-machined components can be repaired rapidly, considerable savings in materials, processing time, and costs can be achieved.

Laser additive manufacturing (LAM) [7] has attracted much attention in the past ten years. By combining laser cladding with rapid prototyping techniques, LAM is an advanced fabrication technique for producing fully dense near-net-shape metallic components on metallic substrates [8]. Based on LAM, laser additive repairing (LAR) technology has been developed [9–11]. By using the damaged or mis-machined components as substrates, the geometry and mechanical properties of the damaged or mis-machined components can be repaired using LAR without deteriorating

the performance of the body parts. Compared with traditional repair technologies [12–14], such as
electrobrush plating, thermal spraying, and argon arc welding, LAR has the advantages of a high electrobrush plating, thermal spraying, and argon arc welding, LAR has the advantages of a high degree of automation, a small heat a ected zone, metallurgical bonding between the repaired zones and degree of automation, a small heat affected zone, metallurgical bonding between the repaired zones the body part, and a reasonable repair cost [15]. A number of metallic components made of di erent and the body part, and a reasonable repair cost [15]. A number of metallic components made of type of materials, including stainless steel, cobalt-based alloys, titanium alloys, and nickel-based alloys, different type of materials, including stainless steel, cobalt-based alloys, titanium alloys, and
have been repaired using LAR technology [16–18].
nickel-based alloys, have been repaired using LAR technology [16–18].

In recent years, the processing parameters, microstructures, and mechanical properties of Inconel In recent years, the processing parameters, microstructures, and mechanical properties of

625 fabricated using LAM technology have attracted much attention [19–22]. Dinda et al. [23] studied Inconel 625 fabricated using LAM technology have attracted much attention [19–22]. Dinda et al. [23]
the microstructural evolution and structural thermal stability of a LAM Inconel 625 alloy. The results studied the microstructural evolution and structural thermal stability of a LAM Inconel 625 alloy.
indicated that the as-deposited microstructure mostly consisted of columnar dendrites that were stable The results indicated that the as-deposited microstructure mostly consisted of columnar dendrites
up to 1000 C. Rombouts et al. [24] found that Inconel 625 deposited using directed energy deposition that were stable up to 1000 °C. Rombouts et al. [24] found that Inconel 625 deposited using directed
(DED) also showed a microstructure of dendrites parallel to the build direction. Rivera et al. [25] energy deposition (DED) also showed a microstructure of dendrites parallel to the build direction.
observed fine grain structures at the layer interfaces of Inconel 625 produced using solid-state additive Rivera et al. [25] observed fine grain structures at the layer interfaces of Inconel 625 produced using
manufacturing. Compared to samples fabricated using LAM, not only the microstructures of the solid-state additive manufacturing. Compared to samples fabricated using LAM, not only the
repaired part, but also the microstructures of the interface between the substrate and the repaired microstructures of the repaired part, but also the microstructures of the interface between the
part, are essential to the mechanical properties of the component repaired using LAR. The research substrate and the repaired part, are essential to the mechanical properties of the component repaired
work of LAR for nickel-based alloys mainly focuses on the repair defects, processing parameters, using LAR. The research work of LAR for nickel-based alloys mainly focuses on the repair defects,
microstructures, and mechanical properties of repaired samples. Onuike et al. [10] used DED technology processing parameters, microstructures, and mechanical properties of repaired samples. Onuike et
to repair the internal cracks in Inconel 718 alloy. Sui et al. [9] studied the tensile deformation behavior of al. [10] used DED technology to repair the internal cracks in Inconel 718 alloy. Sui et al. [9] studied
LARed Inconel 718 alloy with a non-uniform microstructure. To the best of our knowledge, no studies the tensile deformation behavior of LARed Inconel 718 alloy with a non-uniform microstructure. To
have investigated the relationship between the microstructure and micro-mechanical properties of the best of our knowledge, no studies have investigated the relationship between the microstructure
LARed Inconel 625 alloy around the repaired interface.
and micro-mechanical properties of LARed Inconel 625 alloy around the repaired interface.

In order to explore the potential of LAR as a reliable repair solution for damaged and mis-machined In order to explore the potential of LAR as a reliable repair solution for damaged and

Inconel 625 components, Inconel 625 alloy substrates, with premade trapezoidal groove shaped defects, mis-machined Inconel 625 components, Inconel 625 alloy substrates, with premade trapezoidal
were repaired using LAR in this study. The microstructures around the repaired interface and the groove shaped defects, were repaired using LAR in this study. The microstructures around the
corresponding mechanical properties were investigated.
repaired interface and the corresponding mechanical properties were investigated.

2. Materials and Methods

2. Materials and Methods

2.1. Materials
2.1. Materials
The raw materials were prealloyed Inconel 625 powders prepared using a plasma rotating
The raw materials were prealloyed Inconel 625 powders prepared using a plasma rotating electrode process. These powders had spherical shapes with sizes of 75~125 m, as shown in Figure 1a.
electrode process. These powders had spherical shapes with sizes of 75 ~ 125 μm, as shown in Figure The microstructure of the powders showed a fine dendritic morphology on the surface, which
1a. The microstructure of the powders showed a fine dendritic morphology on the surface, which was caused by the rapid solidification during atomization (Figure 1b). Before the LAR experiment,
was caused by the rapid solidification during atomization (Figure 1b). Before the LAR experiment, the powders were dried in a vacuum oven at 120 10 C for 2 h. The LAR process was performed on
the powders were dried in a vacuum oven at 120 ± 10 °C for 2 h. The LAR process was performed on heat treated wrought Inconel 625 substrate, for which the chemical composition is listed in Table 1.
heat treated wrought Inconel 625 substrate, for which the chemical composition is listed in Table 1.
The chemical composition of Inconel 625 powder is also listed in Table 1.
The chemical composition of Inconel 625 powder is also listed in Table 1.

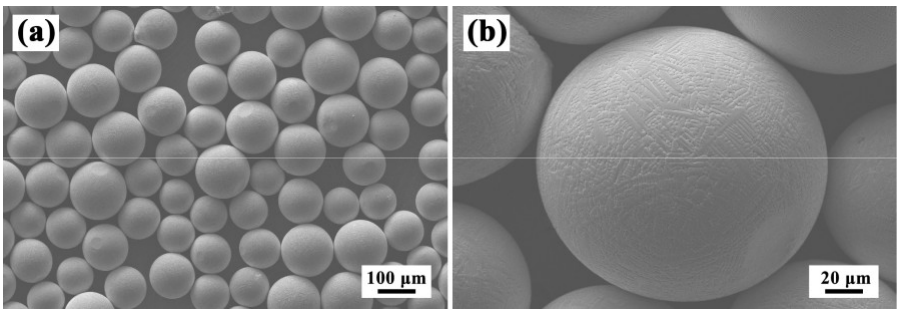

Figure 1. Morphologies of Inconel 625 powders at (**a**) low and (**b**) high magnifications.
Figure 1. Morphologies of Inconel 625 powders at (**a**) low and (**b**) high magnifications.

Table 1. The chemical compositions (wt %) of Inconel 625 alloy powder and substrate.

Material	Ni	Cr	Mo	Nb	Fe	Ti	Al	C	Co	Mn	Si	P
Powder	Bal.	21.92	9.09	3.62	3.71	0.20	0.17	0.036	0.009	0.015	0.06	0.003
Substrate	Bal.	21.70	8.90	3.27	4.40	0.18	0.12	0.030	0.010	0.170	0.15	0.008

Table 1. The chemical compositions (wt %) of Inconel 625 alloy powder and substrate.

Material	Ni	Cr	Mo	Nb	Fe	Ti	Al	C	Co	Mn	Si	P
Powder	Bal.	21.92	9.09	3.62	3.71	0.20	0.17	0.036	0.009	0.015	0.06	0.003
Substrate	Bal.	21.70	8.90	3.27	4.40	0.18	0.12	0.030	0.010	0.170	0.15	0.008

2.2. Experimental Procedures

The LAR experiments were performed on a LAM system (LAM, LSF-12000, Nanjing, China), which consists of a fiber laser with a wavelength of 1070 nm, a five-axis numerical control working table, a powder feeder system with a coaxial nozzle, and an inert atmosphere glove box (oxygen content ≤ 10 ppm). Argon gas was used to protect the molten pool from oxidation and deliver the alloy powders. The LAR process was performed on the substrate with a pre-machined groove defect, as shown in Figure 2a. Then the defect was repaired layer by layer using the LAM system, as shown in Figure 2b. Figure 3 shows a schematic of the scanning strategy of the LAR process. The scanning directions in the same layer followed a zigzag pattern, and were rotated by 90 degree in the following layer. The process parameters are listed in Table 2.

A tensile testing bar was cut from the repaired sample by spark erosion. The volume fraction of the repair zone in the cross-section of the tensile testing bar was 50%, as shown in Figure 2c,d.

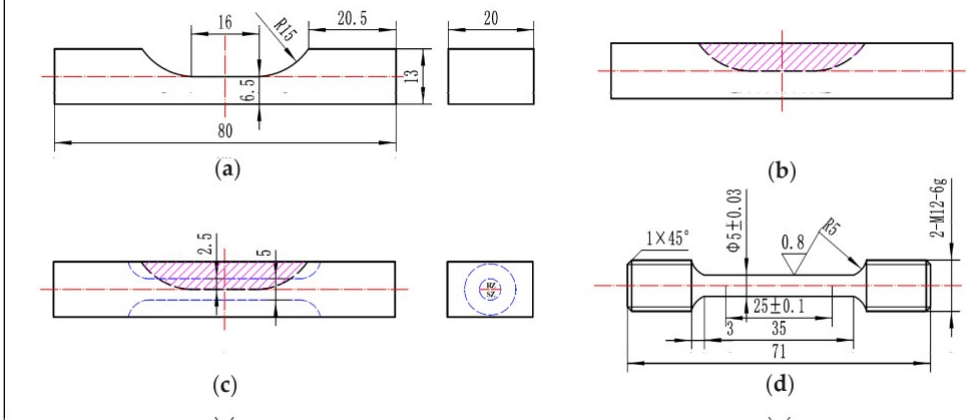

Figure 2. Sketch of (**a**) substrate with pre-machined groove defect, (**b**) LARed sample, (**c**) the position **Figure 2.** Sketch of (**a**) substrate with pre-machined groove defect, (**b**) LARed sample, (**c**) the position **Figure 2.** Sketch of (**a**) substrate with pre-machined groove defect, (**b**) LARed sample, (**c**) the position of the tensile testing bar in the LARed sample, and (**d**) shape and size of the tensile testing bar.
of the tensile testing bar in the LARed sample, and (**d**) shape and size of the tensile testing bar.
of the tensile testing bar in the LARed sample, and (**d**) shape and size of the tensile testing bar.

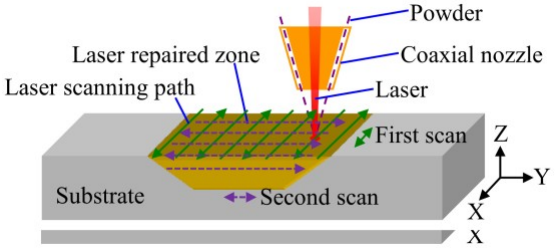

Figure 3.. Schematic of the scanning strategy of the LAR process..
Figure 3. Schematic of the scanning strategy of the LAR process.
Table 2. Process parameters of LARed Inconel 625 alloy.
Table 2. Process parameters of LARed Inconel 625 alloy.

Table 2. Process parameters of LARed Inconel 625 alloy.

Laser Power (kW)	Scanning Speed (mm/min)	Laser Spot Diameter (mm)	Increment of Z Axis (mm)	Powder Feeder Rate (g/min)	Overlaps (%)
Laser Power (kW)	Scanning Speed (mm/min)	Laser Spot Diameter (mm)	Increment of Z Axis (mm)	Powder Feeder Rate (g/min)	Overlaps (%)
Power	Speed	Laser Spot	Increment of	Powder Feeder	Overlaps
1.4	(mm/min)$_{400}$	Diameter$_3$ (mm)	Z Axis$_{0.5}$ (mm)	Rate$_6$ (g/min)	$_{45}$(%)
Power (kW)	(mm/min)	Diameter (mm)	Z Axis (mm)	Rate (g/min)	(%)
(kW)					
1.4	400	3	0.5	6	45
1.4	400	3	0.5	6	45

A tensile testing bar was cut from the repaired sample by spark erosion. The volume fraction of

the repaiMicrostructureszoneinthe crossand-stectionxturesof aroundthetensilethetestingrepairedbarwasinterface50%,as wereshownexaminedFigure 2bycd.optical Microstructures and textures around the repaired interface were examined by optical metallogMicrostructuresaphy(OM, OlympusandtexturesOLS4000,aroundTokyo,the Japan),repairedscainningterfaceelectronwere microscopyexamined by(SEM,opticalFEI metallography (OM, Olympus OLS4000, Tokyo, Japan), scanning electron microscopy (SEM, FEI mHetallogrliosNanolabphy(OM,600i,OlympusHillsboro,OLS4000,OR,USA),Tokyo,andJapan),electronscanningbackscatteredelectronmicroscopydiffraction(SEM, (EBSD,FEIEDAX,Helios Helios Nanolab 600i, Hillsboro, OR, USA), and electron backscattered diffraction (EBSD, EDAX, Mahwah, NJ, USA). Elemental analysis was carried out using energy-dispersive X-ray spectrometry Mahwah, NJ, USA). Elemental analysis was carried out using energy-dispersive X-ray spectrometry (EDS, EDAX, Mahwah, NJ, USA). Before the microstructure observation, samples were ground on (EDS, EDAX, Mahwah, NJ, USA). Before the microstructure observation, samples were ground on 500-2000 grit silicon carbide papers and mechanically polished. Polished samples were then electro 500-2000 grit silicon carbide papers and mechanically polished. Polished samples were then electro etched under an 8 V direct current (DC) for 15 s in a reagent of 10% aqueous chromic acid solution to etched under an 8 V direct current (DC) for 15 s in a reagent of 10% aqueous chromic acid solution to Nanolab 600i, Hillsboro, OR, USA), and electron backscattered di raction (EBSD, EDAX, Mahwah, NJ, USA). Elemental analysis was carried out using energy-dispersive X-ray spectrometry (EDS, EDAX, Mahwah, NJ, USA). Before the microstructure observation, samples were ground

on 500–2000 grit silicon carbide papers and mechanically polished. Polished samples were then electro etched under an 8 V direct current (DC) for 15 s in a reagent of 10% aqueous chromic acid solution to reveal the microstructure. All EBSD samples were polished using an argon beam under a voltage of 5 kV and a current of 110 A for 20 min before the EBSD test. The EBSD test used a voltage of 20 kV and a step size of 1 m. X-ray di raction (XRD, TDF-3000, Dandong, China) scanning was carried out at a constant scanning speed of 10 /min with Cu K radiation, and recorded in 2 ranging from 30 to 100 . To identify tiny phases in the microstructures, a transmission electron microscope (TEM, FEI Titan G2 60-300, Hillsboro, OR, USA) equipped with EDS was applied. The TEM samples, with a 3 mm diameter disc shape, were prepared by mechanical grinding to ~50 m and then twin-jet polished in a solution of 250 mL $HCLO_4$+750 mL methanol at a temperature of 30 C and a voltage of 25 V. Vickers hardness of the samples was tested under a load of 200 g and a duration time of 15 s along the deposition direction. The elastic modulus and microhardness of di erent zones were evaluated by nano-indentation (Hysitron TI-950, Minneapolis, MN, USA) under a load of 5 mN. The room temperature tensile properties of the LARed samples and substrates were tested using a floor model universal testing system (CMT5105, Jinan, China), at a displacement rate of 2 mm/min. For each tensile test condition, three samples were used to calculate the average values and standard deviations of strengths, elongations, and area reductions. The ultimate tensile strength, 0.2% o set yield strength and elongation, was obtained from the resulting stress-strain curves, and the area reduction was determined by measuring the cross-sectional area before and after failure. The fracture morphology was observed using SEM.

3. Results and Discussion

3.1. Microstructure Around the Repaired Interface

3.1.1. Grain Structures

Figure 4a–d show the microstructures in the X–Z section and Y–Z section of the LARed samples around the repaired interface, respectively. The interface between the substrate and the repaired zone presents good metallurgical bonding. No obvious defects, such as cracks and pores can be observed. A transition of microstructure can be observed along the deposition direction, dividing the area into three zones: the substrate zone (SZ), the heat-a ected zone (HAZ), and the repaired zone (RZ) (see Figure 4b,d). Inside the RZ, a narrow overlapping transition zone (OTZ) can be observed, between two adjacent deposited layers or tracks (see Figure 4b,d). The width of the OTZ is approximately 0.15 mm. The SZ consists of a mixture of finely and large equiaxed grains. The grains in the HAZ are hard to reveal under the same erosion conditions, suggesting a composition variation in grain boundaries. Detailed grain structure observation was carried out using EBSD, as in the following. RZ presents a columnar dendritic structure that grows epitaxially along the deposition direction. In addition, the dendritic structure in the OTZ between two adjacent deposited tracks is coarser than other areas in the RZ.

Detailed investigations on the microstructures around the repaired interface of the LARed Inconel 625 were carried out using EBSD. Figure 5a–d show the EBSD images in the X–Z section and Y–Z section of the LARed samples around the repaired interface, respectively. The three zones of SZ, HAZ, and RZ can be easily distinguished in the EBSD images, showing grains with different sizes and distributions. The SZ has typical equiaxed grains, with a bimodal grain size distribution. Annealing twins can be observed in the recrystallized grains. Grains in the HAZ grew significantly larger compared to those in the SZ. In the RZ, large sized columnar grains grew epitaxially from the mother grains in the HAZ. The height of the columnar grains can be as large as the layer height. The widths and heights of the columnar grains increase as the deposition height increases. The OTZ cannot be observed in the EBSD maps.

approximately 0.15 mm. The SZ consists of a mixture of finely and large equiaxed grains. The grains in the HAZ are hard to reveal under the same erosion conditions, suggesting a composition variation in grain boundaries. Detailed grain structure observation was carried out using EBSD, as in the following.

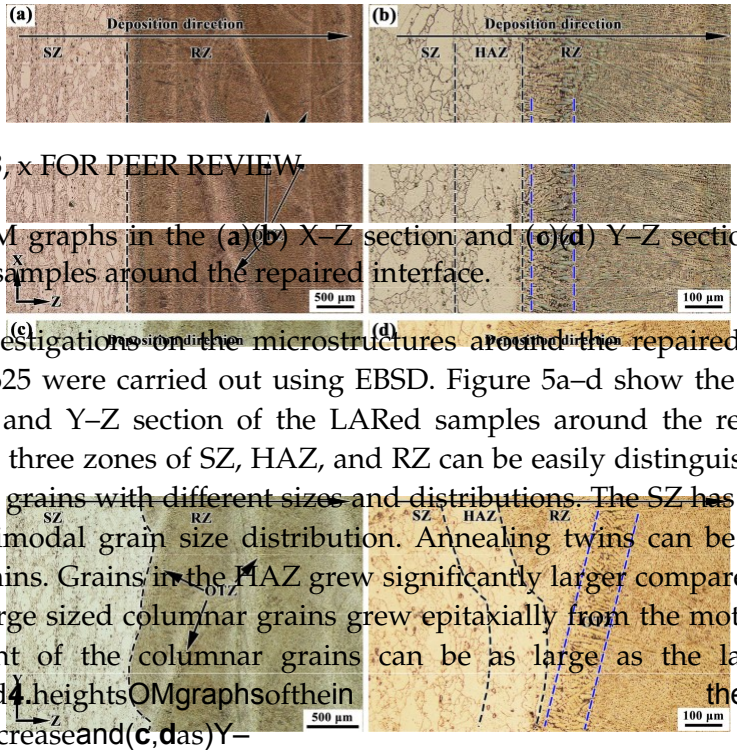

Figure 4. OM graphs in the (**a**)(**b**) X–Z section and (**c**)(**d**) Y–Z section of LARed Inconel 625 samples around the repaired interface.

Detailed investigations on the microstructures around the repaired interface of the LARed Inconel 625 were carried out using EBSD. Figure 5a–d show the EBSD images in the X–Z section and Y–Z section of the LARed samples around the repaired interface, respectively. The three zones of SZ, HAZ, and RZ can be easily distinguished in the EBSD images, showing grains with different sizes and distributions. The SZ has typical equiaxed grains, with a bimodal grain size distribution. Annealing twins can be observed in the recrystallized grains. Grains in the HAZ grew significantly larger compared to those in the SZ. In the RZ, large sized columnar grains grew epitaxially from the mother grains in the HAZ. The height of the columnar grains can be as large as the layer height. The widths and heights of the columnar grains increase as the layer height increases. The OTZ cannot be observed in the EBSD maps.

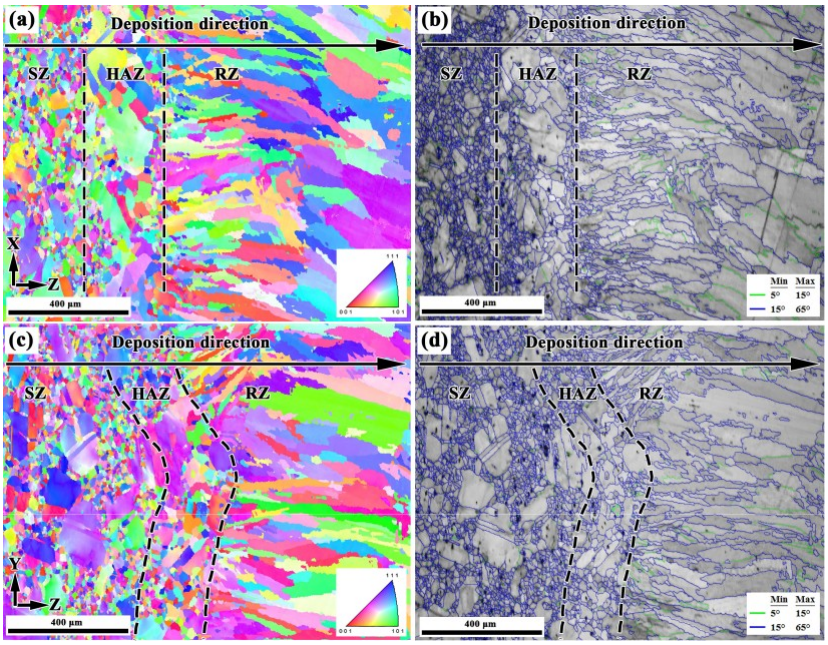

Figure 5. EBSD results of the LARed Inconel 625 samples around the repaired interface in the (**a**)(**b**)

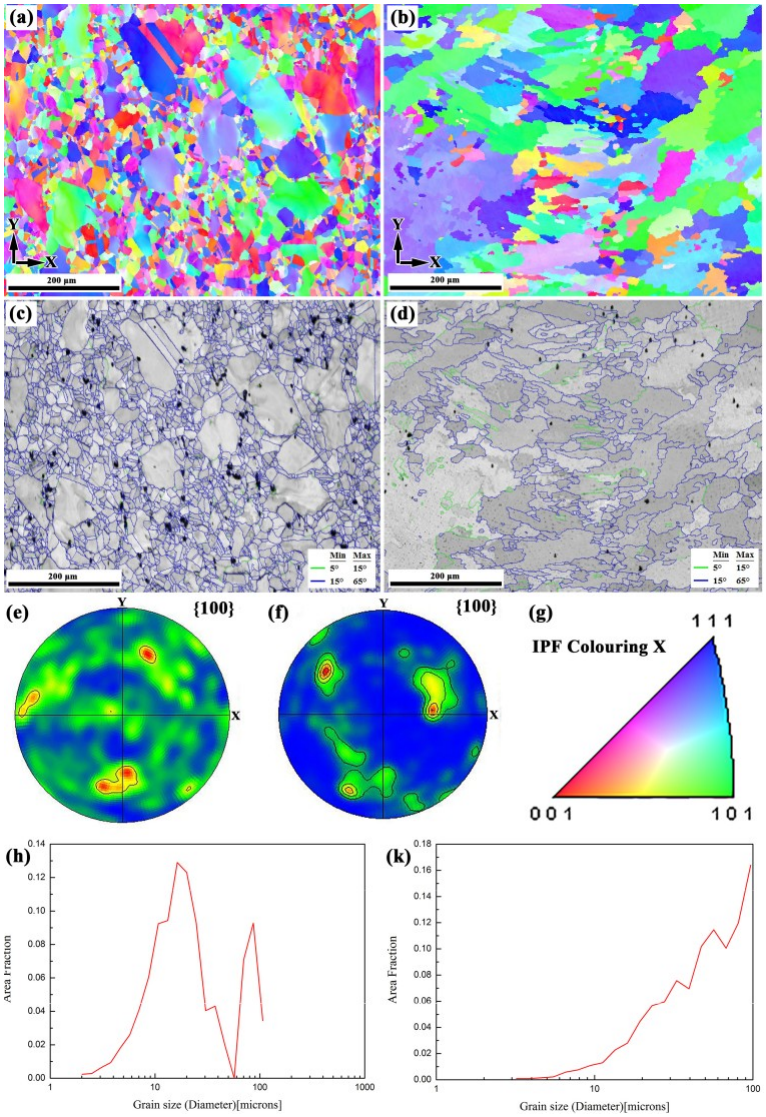

Figure 6. EBSD results of LARed Inconel 625 samples of the substrate zone (SZ) (**a**)(**c**)(**e**)(**h**) and the **Figure 6.** EBSD results of LARed Inconel 625 samples of the substrate zone (SZ) (**a**,**c**,**e**,**h**) and the repaired zone (RZ) (**b**)(**d**)(**f**)(**k**) in the X–Y section: (**a**)(**b**) IPF orientation maps, (**c**)(**d**) band contrast repaired zone (RZ) (**b**,**d**,**f**,**k**) in the X–Y section: (**a**,**b**) IPF orientation maps, (**c**,**d**) band contrast maps, maps, (**e**)(**f**) {100} pole figures, (**g**) IPF and (**h**)(**k**) grain size distribution. (**e**,**f**) {100} pole figures, (**g**) IPF and (**h**,**k**) grain size distribution.

3.1[3].2[.1]. [.2]Phases[.es]and[and]Precipitations

Figure 7 shows the X-ray diffraction patterns of the RZ and SZ in the repaired sample. It can be Figure 7 shows the X-ray di raction patterns of the RZ and SZ in the repaired sample. It can be demonstrated that the RZ and SZ in the LARed samples both mainly consist of the γ (Ni–Cr) phase demonstrated that the RZ and SZ in the LARed samples both mainly consist of the (Ni–Cr) phase without peaks from other precipitates [26], such as0 γ′ (Ni3Al(Ti)), γ″ (Ni3Nb), δ (Ni3Nb), Laves (Ni, without peaks from other precipitates [26], such as (Ni$_3$Al(Ti)), ” (Ni$_3$Nb), (Ni$_3$Nb), Laves (Ni, Fe, Fe, Cr)2(Nb, Ti, Mo), and carbide phases, due to their low volume fractions or absences. Cr)$_2$(Nb, Ti, Mo), and carbide phases, due to their low volume fractions or absences. Furthermore, Furthermore, the diffraction peak intensity of the (200) crystal plane of the γ phase in the RZ is the di raction peak intensity of the (200) crystal plane of the phase in the RZ is higher than that of higher than that of the (111) crystal plane, which also indicates that the microstructure in the RZ has the (111) crystal plane, which also indicates that the microstructure in the RZ has a strong texture.

a strong texture.

Detailed SEM investigations were applied to the areas around the repaired interface. Figure 8

Detailed SEM investigations were applied to the areas around the repaired interface. Figure 8

shows SEM images of the SZ. A large number of precipitates can be seen in the grain boundaries and

shows SEM images of the SZ. A large number of precipitates can be seen in the grain boundaries and

grain interior (Figure 8a,b). The precipitates have two typical average sizes of 10 m and 0.5 m.

grain interior (Figure 8a, b). The precipitates have two typical average sizes of 10 μm and 0.5 μm.

The large precipitates mainly have irregular shapes. The small precipitates have both flocculent shapes

The large precipitates mainly have irregular shapes. The small precipitates have both flocculent and polygonal shapes (see Figure 8c). The chemical compositions of the matrix (as indicated by point

shapes and polygonal shapes (see Figure 8c). The chemical compositions of the matrix (as indicated

precipitates mainly comprised Nb and Ti, while the matrix was rich in Ni and Cr but depleted in Nb

comprised Nb and Ti, while the matrix was rich in Ni and Cr but depleted in Nb and Ti. The results

and Ti. The results indicate that Nb and Ti in the matrix were segregated to form large precipitates.

indicate that Nb and Ti in the matrix were segregated to form large precipitates. These large precipitates

These large precipitates were assumed to be MC-type carbides (M is Nb or Ti), while the matrix was

were precipitatesassumedtomainlybeMCcomprised-typecarbidesNbandMTi,iswhileNbortheTi),matrixwhilewastherichmatrixinNiwasandassumedCrbutdepletedtobeain Nb(Ni-Cr)

assumedand Tito.Thebe resultsay indicate(Ni-Cr) thatsolidNb solutionandTiin. theTEMmatrixobservationsweresegregatedandtotheformequippedlargeprecipitatesEDSX.-ray

solid solution. TEM observations and the equipped EDS X-ray microanalysis were carried out to clarify

microanalysisTheselargewereprecipitatescarriedwereoutassumedtoclarifyto betheMCsmall-type preccarbidespitates(Mis(shownNborTi),inwhileFigurethe 8ematrix–f). Thewas EDS

the small precipitates (shown in Figure 8e,f). The EDS analysis results revealed that the polygonal

analysis[assumed]results[to] revealed[bey] [(Ni]that[-Cr)]the[solid]polygonal[solution]shaped[.TEM] precipitate[observations]was[and]NbC,[the equipped]andtheflocculent[EDSX-ray]phase shaped precipitate was NbC, and the flocculent phase was a Laves phase, which is consistent with the

microanalysis were carried out to clarify the small precipitates (shown in Figure 8e–f). The EDS was a Laves phase, which is consistent with the observations made by Xu [27].

observations made by Xu [27].

analysis results revealed that the polygonal shaped precipitate was NbC, and the flocculent phase was a Laves phase, which is consistent with the observations made by Xu [27].

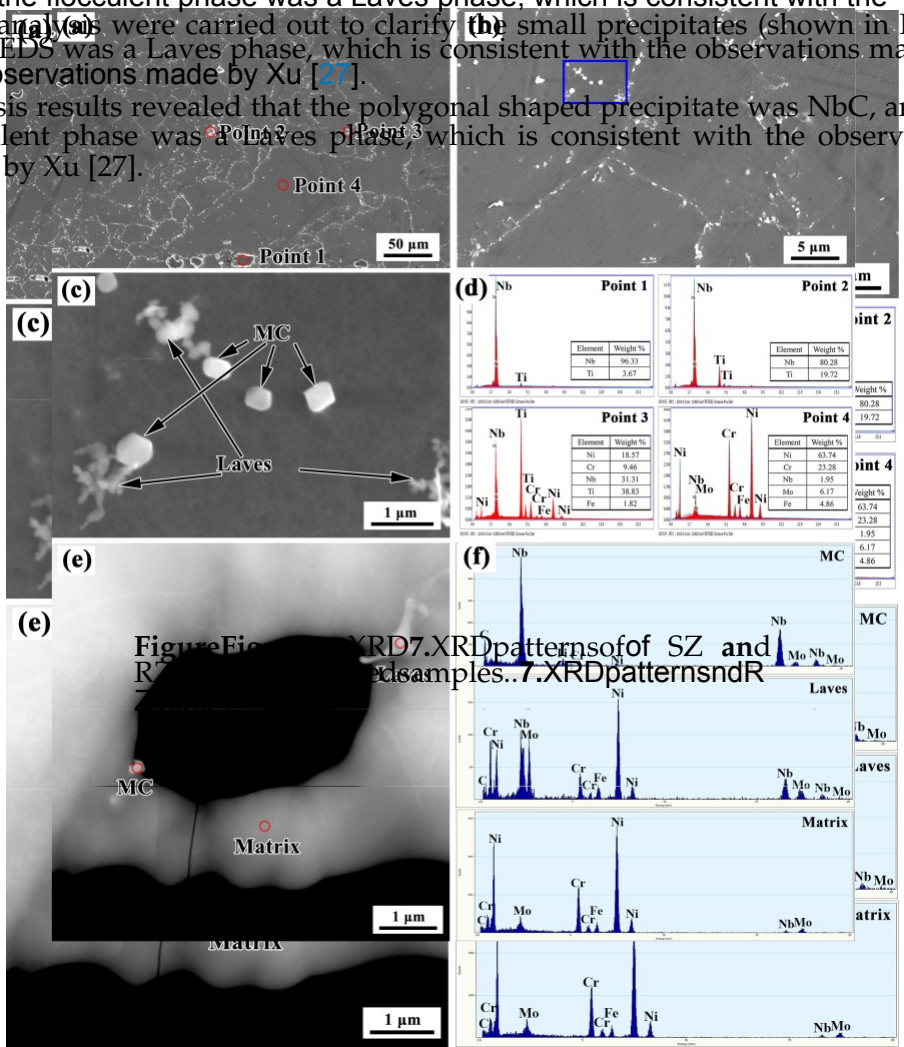

Figure 7. XRD patterns of SZ and R[illegible] samples.

7. XRD patterns of SZ and R[illegible] samples.

Figure 8. (**a**–**c**) SEM images, (**e**) transmission electron microscope (TEM) images, and (**d**,**f**) energy-dispersive X-ray spectrometry (EDS) results in the SZ.

Figure 8. (**a**–**c**) SEM images, (**e**) transmission electron microscope (TEM) images, and (**d**,**f**)

Figure 9a presents the microstructure of repaired samples around the repaired interface. The Figure 9a presents the microstructure of repaired samples around the repaired interface. microstructure is quite different in the SZ and the RZ along the deposition direction. Similarly to the The microstructure is quite di erent in the SZ and the RZ along the deposition direction. Similarly SZ, a large amount of white precipitates are also seen in the HAZ and RZ. From the previous to the SZ, a large amount of white precipitates are also seen in the HAZ and RZ. From the previous analysis, we can see that the precipitates of the SZ mainly consist of large (approximately 10 μm) analysis, we can see that the precipitates of the SZ mainly consist of large (approximately 10 m) irregular shaped MC-type carbides (M is Nb and Ti), small (approximately 0.5 μm) polygonal irregular shaped MC-type carbides (M is Nb and Ti), small (approximately 0.5 m) polygonal shaped shaped MC-type carbides, and flocculent shaped Laves phase. In the HAZ, there are still many large MC-type carbides, and flocculent shaped Laves phase. In the HAZ, there are still many large irregular irregular shaped MC-type carbides, but some small sized precipitates dissolved in the original grain shaped MC-type carbides, but some small sized precipitates dissolved in the original grain boundaries,
boundaries, as shown in Figure 9b.
as shown in Figure 9b.
For the RZ, the microstructure indicates epitaxial growth of the columnar dendritic structure, For the RZ, the microstructure indicates epitaxial growth of the columnar dendritic structure, and a large amount of white precipitates occur along the dendritic boundaries, as shown in Figure and a large amount of white precipitates occur along the dendritic boundaries, as shown in Figure 9a. 9a. In addition, compared to the microstructure in the layer interior, the amount of precipitates is In addition, compared to the microstructure in the layer interior, the amount of precipitates is greater, greater, and the size is largest in the OTZ around the repaired interface, as shown in Figure 9cd. The and the size is largest in the OTZ around the repaired interface, as shown in Figure 9c,d. The precipitates precipitates mainly have flocculent shapes. Figure 9f shows the EDS analysis results of the flocculent
mainly have flocculent shapes. Figure 9f shows the EDS analysis results of the flocculent shaped phase shaped phase and the matrix phase. The results of the EDS analysis reveal that the main hardening
and the matrix phase. The results of the EDS analysis reveal that the main hardening elements Nb elements Nb and Mo are rich in the flocculent shaped phase, which is the characteristic Laves phase
and Mo are rich in the flocculent shaped phase, which is the characteristic Laves phase of Inconel 625 of Inconel 625 alloys [28,29]. This indicates a somewhat heavy segregation in the OTZ. Figure 10 alloys [28,29]. This indicates a somewhat heavy segregation in the OTZ. Figure 10 further shows the further shows the high resolution transmission electron microscopy (HRTEM) image and the EDS
high resolution transmission electron microscopy (HRTEM) image and the EDS results of nanosized results of nanosized precipitates in the RZ. The EDS analysis indicates that it is NbC. Therefore, the
precipitates in the RZ. The EDS analysis indicates that it is NbC. Therefore, the precipitates of the RZ precipitates of the RZ mainly consist of the flocculent shaped Laves phase and a small amount of mainly consist of the flocculent shaped Laves phase and a small amount of nanosized MC-type carbides. nanosized MC-type carbides.

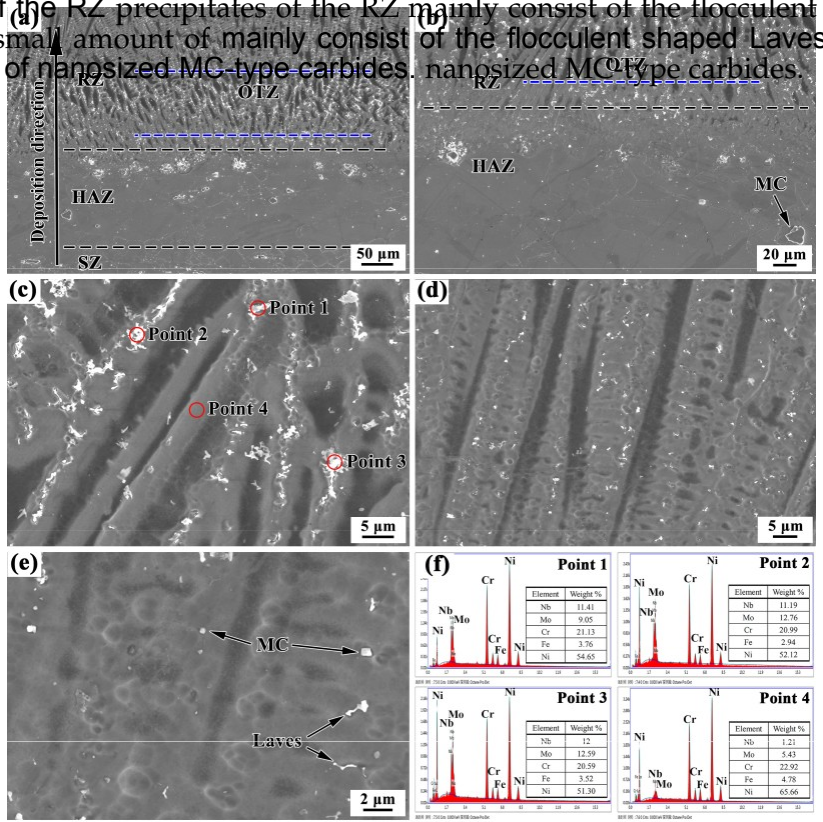

Figure 9. Microstructures of LARed samples in different zones: (**a**) SZ+heat-affected zone (HAZ)+RZ,
Figure 9. Microstructures of LARed samples in di erent zones: (**a**) SZ+heat-a ected zone (HAZ)+RZ,
(**b**) HAZ+RZ, (**c**) overlapping transition zone (OTZ), (**d**, **e**) RZ, and (**f**) EDS taken from laves phase (**b**) HAZ+RZ, (**c**) overlapping transition zone (OTZ), (**d**,**e**) RZ, and (**f**) EDS taken from laves phase and
and matrix phase of OTZ around the repaired interface.
matrix phase of OTZ around the repaired interface.

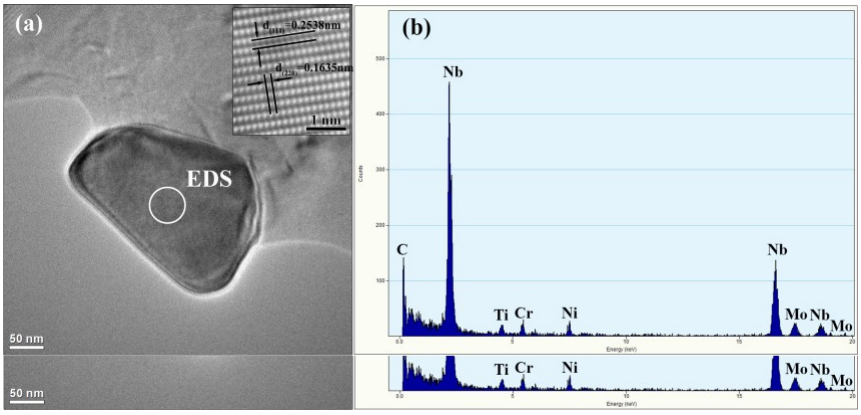

Figure 10. HRTEM images (**a**) of LARed samples in the RZ, and (**b**) the EDS results of a NbC precipitate.

Figure**re 10.** HRTEM images (**a**) of LARed samples in the RZ, and (**b**) the EDS results$_{precipitate}$ofNbC

10. HRTEM images (**a**) of LARed samples in the RZ, and (**b**) the EDS results of a NbC .

precipitate.

3.1.3. Microstructure in the Overlapping Transition Zone

3.1.3. Microstructure in the Overlapping Transition Zone

3.1.3.FiguMicrostructure11showsinthethemicrostructureOverlappingTransitionoftheOTZonebetween two adjacent deposited tracks in the Figure 11 shows the microstructure of the OTZ between two adjacent deposited tracks in the RZ.

RZ. Similarly to the OTZ around the repaired interface, the microstructure of the OTZ in the RZ also Similarly to the OTZ around the repaired interface, the microstructure of the OTZ in the RZ also presents Figure 11 shows the microstructure of the OTZ between two adjacent deposited tracks in the presents a coarse columnar dendritic structure in Figure 11a. The width of the OTZ is also a coarse columnar dendritic structure in Figure 11a. The width of the OTZ is also approximately 0.15 RZ. Similarly to the OTZ around the repaired interface, the microstructure of the OTZ in the RZ also approximately 0.15 mm. Particularly, a large amount of white precipitates occur along the dendritic mm. Particularly, a large amount of white precipitates occur along the dendritic boundaries in the presents a coarse columnar dendritic structure in Figure 11a. The width of the OTZ is also boundaries in the OTZ, as shown in the Figure 11b. The EDS results of the precipitates demonstrate OTZ, as shown in the Figure 11b. The EDS results of the precipitates demonstrate that they are Laves approximately 0.15 mm. Particularly, a large amount of white precipitates occur along the dendritic

that they are Laves phase, as shown in Figure 11c,d.

phase, as shown in Figure 11c,d.

boundaries in the OTZ, as shown in the Figure 11b. The EDS results of the precipitates demonstrate that they are Laves phase, as shown in Figure 11c,d.

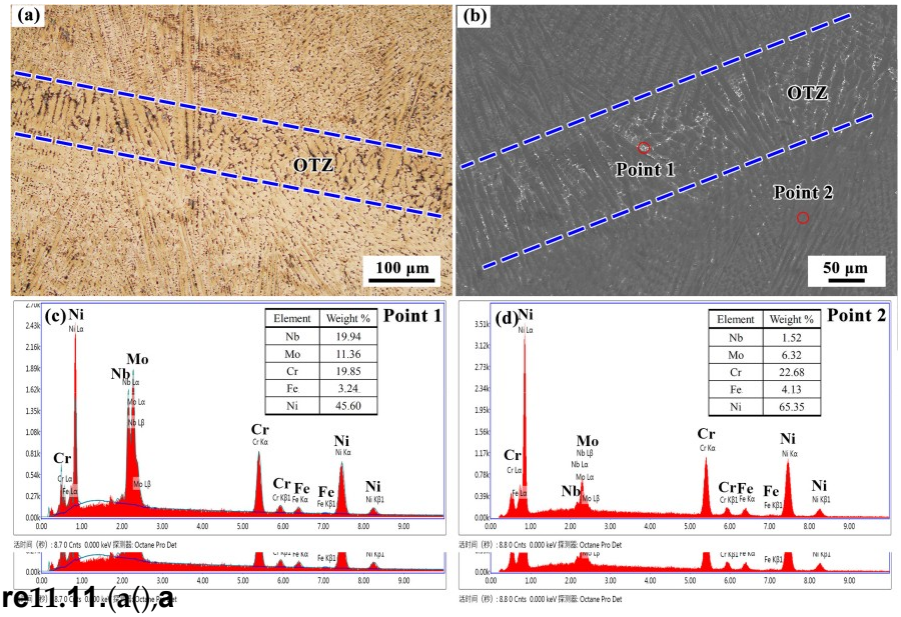

Figure 11. (**a**,**b**) Microstructures of OTZ and the (**c**) EDS results of Laves and (**d**) matrix phases.

Figure 11. (**a**), (**b**) Microstructures of OTZ and the (**c**) EDS results of Laves and (**d**) matrix phases.

The microstructural characteristics between the OTZ and layer interior are quite different, which can be explained by the classical theoretical model of dendrite growth during the solidification microstructure. The Kurz, Giovanola, Trivedi (KGT)model has often been utilized to investigate how the *G* and *R* affect the primary dendritic spacing of a deposited metal [30]. According to the KGT model, the variation of dendritic tip radius *r* with the growth rate *R* of a Ni-based alloy can be described as follows [31]:

$$r = \pi \frac{\Gamma}{k\Delta T} \sqrt{\frac{4D_L}{R}}, \quad (1)$$

where Γ is the Gibbs–Thomson coefficient, D_L is the liquid inter-diffusion coefficient, k is the equilibrium diffusion coefficient, ΔT is the non-equilibrium solidification range. Furthermore, according to Kurz and Fisher analysis [32], the primary dendritic spacing can be expressed by a function of the dendritic tip radius r as [33]:

according to the Kurz and Fisher analysis [32], the primary dendritic spacing λ can be expressed by a

function of the dendritic tip radius r as [33]:

$$\lambda = r\sqrt{\frac{3\Delta T}{G}}, \quad (2)$$

Therefore, the primary dendritic spacing λ is identified as a function of temperature gradient G and the growth rate R as follows:

$$\lambda = \left(\frac{3\pi}{4}\right)^{1/2}\left(\frac{4D_L\Delta T}{G^2}\right)^{1/4}R^{-1/4}, \quad (3)$$

The product $G \cdot R$ (cooling speed) governs the size of the solidification structure [34]. Thus, difference in the temperature gradient G and the growth rate R during the LAR process should be the primary reason for the different morphologies in the OTZ. During the LAR process, the material is deposited track-by-track and layer-by-layer. When a new track is deposited, the top portion of the material in the previous track is remelted, and then forms a molten pool, as shown in Figure 12. The temperature of the previous track is higher than that of the previous layer, therefore, the temperature gradient at the overlapping line, G_1, is less than at the other fusion line, G_2. Consequently, the $G \cdot R$ (cooling rate) is lower at the overlapping line and higher at the other fusion line. This leads to a significant increase in the primary dendritic spacing λ along the overlapping line of the molten pool, which forms an OTZ between tracks.

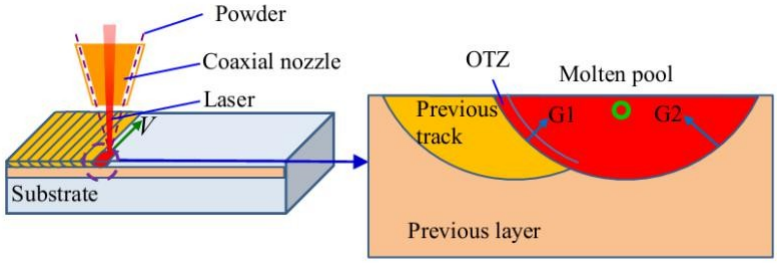

Figure 12. Schematic illustration of the temperature gradient, G, and growth rate, R, distribution in **Figure 12.** Schematic illustration of the temperature gradient, G, and growth rate, R, distribution in the themoltenmoltenpoolpoolduringduringthetheLARLARprocess.process.

ThesizeofoftheLavesphasesisisatttributedtotoththe concentrationofof the alloyingoying elementsents.. During theLARprocesss,solidificationsolidificationinintheInconel625alloystartswiththetheprimaryli quid→!γ reaction, causing the **accumulation** of Nb,Mo,Mo,C,C,andandTi Tiin theintheinterdendriticendriticand andgraingrainboundaryboundaryliquidsliquids.Thus,. Tthus,eLavthesLavesphase phaseandMCand-typeMCcarbides-typecarbidescanprecipitatcanecipitateintheseinregionsthese.regionsThen,the.Then,subsequ entthesubsequentliquid! liquid(+NbC)→(γeutectic+NbC)reactionutecticconsumesreactionconmostumesofthemostca rbofn theavailable,carbonuntilavailable,anotheruntileutecticanothreactionreutecticL! reaction+Laves →occurs,γ+ finishingLavesoccurs,thesolidificationfinshingtheprocesssolidification[27].The Lavesprocessphase[27] .isTheanunLavoidableesphaseterminalisan unavoidsolidificabletionterminalphasein solidificationInconel625alloysphase.However,inInconesolidification625alloys. conditionsHowever, cansolidificationstronglyinfluenceconditionsthe canextentstronglyofniobiuminfluencesegregationtheextentandof niobiumtheamountsegregationofLaves phaseandthe[35amount].Thus,ofa Lavesslowcoolingphase[35]rate. Thus,(GR) ina slowtheOTZcoolingcausesrate a(*G*large·*R*)insegregationtheOTZcausesofthea alloyinglargesegregationelements,ofwthichealleadsoyingtoelements,theformationwhichofleads largeto theamountformationofLavesofa phaselarge.amount of Laves phase.

*3*3.*2*2.·*CompositionDistribution*

TheTheEDSEDSlinelinescanningscanningresultsresultsshowshowthatthatthethemamajoralloyingalloyingelements,elements,suchsuchasNiasandNi Cr,andareCr, distributedaredistributeduniformlyuniformlyfromfromthe thetoSZ toSZ theto theRZ,RZ,as asshownshowninin FigureFigure13[13].·TheThefluctuationsfluctuationsofofsome elementsarearemainlyduedueto tothethedetectionsofofprecprecipitations.·However,thetheNbNbandand MoMoelementsareare distributedmoreuniformlyininthetheRZRZcomparedtotoininthetheSZSZ.·ThisThisisismainlyduedueto tothethesegregationofof NbNbandand Mo elementse ts in the SZ to to form a large amount of of MC MC-type-type carbide carbide and and Laves Laves phases, phases, while while the the degree degree of of segregation regatiofofn the of the alloying alloyingelements in the in the RZ RZ is weak, is and k, and the the precipitated precipitated phase phase is is low In addition, .Intheion, degree thedegr ofs egregationofsegregation ofthealloying ofthe eleme alloying ts is elements aggravated isaggravated intheOTZ in compared theOTZ, to in the layer interior, this is due to Nb and Mo elements segregating and forming a large amount of Laves phase.

compared to in the layer interior, this is due to Nb and Mo elements segregating and forming a large amount of Laves phase.

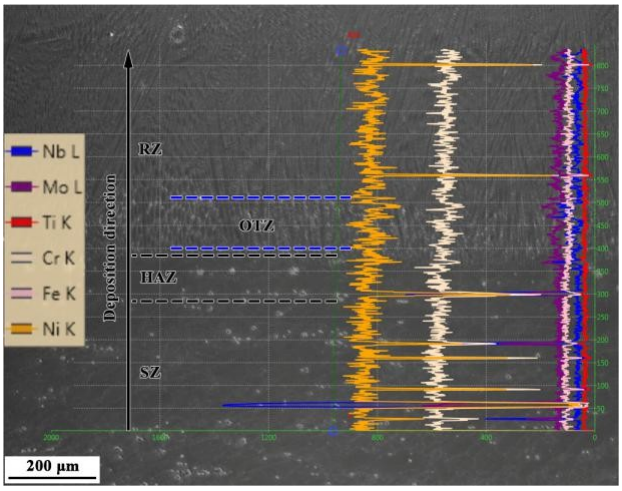

Figure 13. EDS line scanning results of the LARed Inconel 625 alloy sample along the deposition direction.

3.3. Mechanical Properties

3.3.1. Hardness

Figure 14 shows the Vickers hardness along the deposition direction, around the repaired interface.

The hardness values have no notable difference between the SZ and RZ. The average hardness is approximately 240 ± 20 HV. The micro-mechanical properties of the LARed Inconel 625 alloy samples were evaluated using a nanoindentation method for the reduced modulus (E) and microhardness (H) of the LARed Inconel 625 alloy samples were evaluated using a nanoindentation for the reduced modulus (E) and microhardness (H) of different zones around the LARed interface. The nanoindentation load-depth curves of the LARed Inconel 625 alloy in different zones, as shown in Figure 15. The load-depth curves of the LARed Inconel 625 alloy in different zones are predominantly plastic, although some elastic recovery upon release of the load can also be observed. Inconel 625 alloy is small

plateauredominantlycanbeseenplastic,atthealthoughmaximumsomeload,elasticwhichrecovery isindicativeuponreleaseofcrepof inthetheloadInconelcanalso625bealloyobserved.. In bothThefigures,resultantsmallload-depthplateaucurvescanbewerseenusedattheto maxobtaimumnthe Hload,ndwhichErby employingisindicativetheofproceduredreepintheof InconelOliverand625 Pharralloy. [36]. The E_r was then used, together with Poisson's ratio ( ), to calculate the elastic modulusThe resultant(E)from theloadfollowing-depthcurvesequation:were used to obtain the *H* and *Er* by employing the procedure of Oliver and Pharr [36]. The *Er* was then used, together with Poisson's ratio (v), to calculate the

elastic modulus (E) from the following equation:

$$\frac{1}{E_r} = \frac{1 - v^2}{E} + \frac{1 - v_i^2}{E_i}, \quad (4)$$

where E_i and v_i is the elastic modulus of the indenter (1140 GPa) is its Poisson's ratio (0.07) [37]. Furthermore, the Poisson's ratio used for the Inconel 625 alloy was set to 0.303 [38]. The obtained

wh indentationre *E* is themoduluselastic (modulusEr)andmicrohardnessoftheindenter(H(1140)dataGPa)oftheandLARed *vi* isitsIncone lPoisson's625 ratioalloy (0sample.07)[37]in. Furthdierentrmore,zonestheare Poisson'sshownin Figureratioused15b. forThetheEr valuesInconelfor625di alloyerentwaszonessetrevealto0.303imperceptible[38].Theobtchangesined.

Theindentatimicrohardnessmodulusof (the*Er*) matrixandmicrohardnessphaseinthe RZ(*H*)isdataapproximatelyftheLARed5.1 GPa,Inconelwhich625isalloyslightlysamplehigherin differentthanthat ofzonesthe SZare(approximatelyshowninFigure4.8 GPa)15b.. **The**is *E*is*r* duevaluestotheforweakeningdifferet zonesofthe s**r**egregationvealimperceptibleoftheNb changesandMo.alloyingThemicrohardnesselementsintheof RZthe. Inmaddition,trixphasetheinmicrohardnesstheRZisapproximatelyofthematrix5phase.1GPa,in thewhichHAZis slightlygenerallyhigherdemonstratesthanthat lofwerthevalueSZ(ap**p**proximately44.8.6 **GPa**).. **This** is attributeddduetothetoweakeningthedissolutionoftheof segregationtheMC-typeofcarbidetheNbandandLavesMoalloyingphases andelementsthegrowthinthe ofRZthe.Ingrainsaddition,inthetheHAZmicrohardness.Inparticular,of **the** **m**aticrohardnessixphaseinofthe HAZmatrixgenerallyphasein

demonstratestheOTZisapproximatelylowervalue4.7
(approximatelyGPa,whichisslightly4.6GPa)lower.Thisthanis attributedthatoflayerto
intheriordissolutionintheRZof(approximattheMC-
typelycarbide5.1GPa)and.TheLavesformationphases
andofabundantthegrowthLavesofthephasesgrains inthetheOTZHAZisdue.In
toparticular,thelarge thesegregationmicrohardnessofalloyingoftheelematrixents
NbphaseandinMothe.TheOTZLavesisapproximatelyphaseisbrittle4.7
GPa,harmfulwhichphase,is andslightlyconsumeslowr
athanlargethatamountoflayerofNbinteriorandMo,inandthedecreasesRZ(approximatelythea
mount 5of.1 NbGPa)and. TheMo
formationinthematrix,ofabundantwhichleadsLavestothephasesdecreaseintheofOTZthemicr
ohardnessisduetothelargeofthesegregationmatrixphaseofalloyingtheOTZelements.

Nb and Mo. The Laves phase is a brittle harmful phase, and consumes a large amount of Nb and Mo,

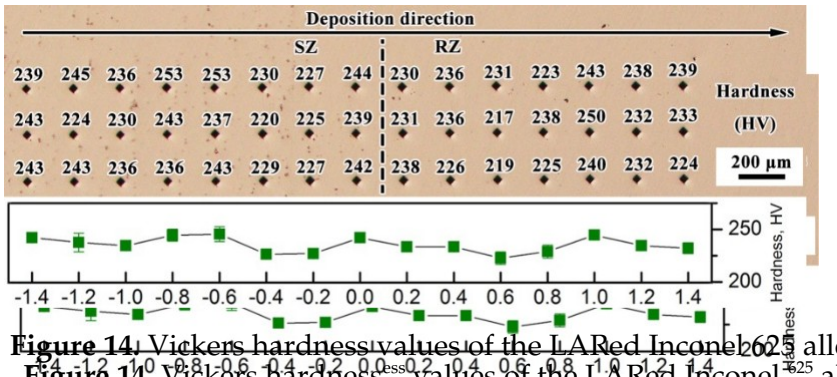

Figure 14. Vickers hardness values of the LARed Inconel 625 alloy sample.
Figure 14. Vickers hardness values of the LARed Inconel 625 alloy sample.

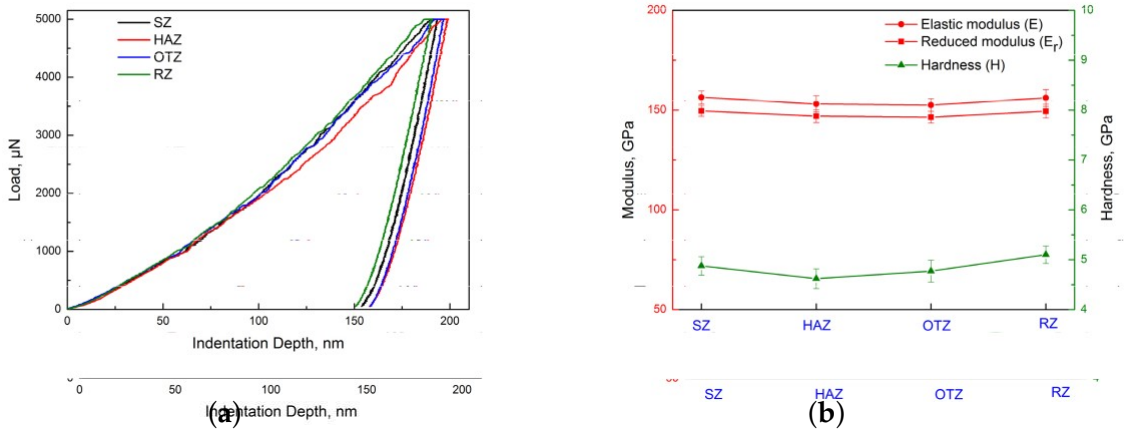

Figure 15. (**a**) Nanoindentation load–depth curves and (**b**) indentation modulus and hardness data of **Figure 15.** (**a**) Nanoindentation load–depth curves and (**b**) indentation modulus and hardness data of (**a**) (**b**) thethematrixmatrixphasephaseinindifferentdier entzoneszonesofofthetheLAReddLAReddsamples.
samples.

Figure 15. (**a**) Nanoindentation load–depth curves and (**b**) indentation modulus and hardness data of $3^{3}.3^{3}.2^{2}$. TensilethematrixTestsphase in different zones of the LARed samples.

The roomtemperaturetensilepropertiesof ththeLAREdsampleand the heattreatedwrought substrateare listedin Table3. The tensilestrengthand ductilityof LAREdsamplesare similarto those of the wroughtsubstrate,whichindicatesthatLARis a reliableapproachfor damagedand mis-machinedcomponentsmadeof theInconel625alloy.

3.3.2. Tensile Tests

The room temperature tensile properties of the LARed sample and the heat treated wrought substrate are listed in Table 3. The tensile strength and ductility of LARed samples are similar to those of the wrought substrate, which indicates that LAR is a reliable approach for damaged and mis-machined components made of the Inconel 625 alloy.

To compare the tensile behaviors of the samples in the various conditions, tensile testing of LARed and wrought samples was done, and the results are shown in Figure 16. The tensile curves of the different samples are almost the same, which indicates that they have similar tensile properties. The wrought substrate demonstrates a slightly steeper elastic response than the

Table 3. Room temperature tensile properties of wrought and LARed Inconel 625 alloy samples.

Number	Ultimate Tensile Strength b (Mpa)	Yield Strength 0.2 (Mpa)	Elongation (%)	Area Reduction Y (%)
test				
of the				
LARed and				
wrought				
Materials				

samplecurves andoftheyieldsdifferentatadifferentsamples stressarealmostlevel .theAftersameyielding,whichtheindicatestensile thatspecimenstheyhaveinallsimilarcases tensileshow LARed sample 908 5 587 3 44.7 0.5 45.0 0.7

properties. The LARed sample demonstrates a slightly steeper elastic response than the wrought

fracture. parallel stress–strain curves in the plastic elongation period before

Wrought substrate 914 4 572 6 45.3 0.4 43.7 0.3

sample and yields at a different stress level. After yielding, the tensile specimens in all cases show almost **Table** parallel **3.** Roomstresstemperature– straincurvestenileinpropertiestheplasticofelongationwroughtandperiodLARedbeforeIncon elfracture625alloy. samples.

To compare the tensile behaviors of the samples in the various conditions, tensile testing of the LARed and wrought samples was done, and the results are shown in Figure 16. The tensile test curves

Ultimate Tensile **Area Table 3.** Room temperature tensile properties of wrought and LARed Inconel 625 alloy samples.

of the di erent samples are almost the same, which indicates **that** they have similar tensile properties.

Number	LARed	Strength	sampleteepero elastic(Mpa)responseδthan(%)	Reduction
The	demonstrates	**Ultimate** slightly **Tensile**	wrought **Area** sample and	the
		.2		

	σb (Mpa)	Yield Strength	Elongation	Ψ (%)
yields at a di erent stress level. After yielding, the tensile specimens in all cases show almost para				llel

Number	Strength	period before	σ587 0.2(Mpa) ±3 fracture.	Reduction
stressLARed–strainsamplecurvs in the				
plastic908elongation±5		44.δ7 ±(%)0.5		45.0 ± 0.7

	σb (Mpa)			Ψ (%)
Wrought substrate	914±4	572±6	45.3 ± 0.4	43.7 ± 0.3
LARed sample	908±5	587±3	44.7 ± 0.5	45.0 ± 0.7
Wrought substrate	914±4	572±6	45.3 ± 0.4	43.7 ± 0.3

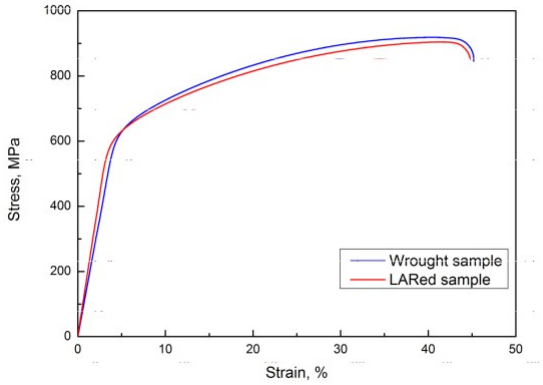

Figure 16. Typical tensile test curves of LARed sample and wrought substrate.

Figure 16. Typical tensile test curves of LARed sample and wrought substrate

Figure 16. Typical tensile test curves of LARed sample and wrought substrate

Figure 17 shows the fractographs of the wrought sample. The fracture surface of the wrought Figure 17 shows the fractographs of the wrought sample. The fracture surface of the wrought

Figure 17 shows the fractographs of the wrought sample. The fracture surface of the wrought sample exhibits fine dimples, which indicate a ductile mode of failure associated with good tensile sample exhibits fine dimples, which indicate a ductile mode of failure associated with good tensile

sample exhibits fine dimples, which indicate a ductile mode of failure associated with good tensile properties. In addition, a large number of secondary cracks can be found. The fractograph of the properties. In addition, a large number of secondary cracks can be found. The fractograph of the

properties. In addition, a large number of secondary cracks can be found. The fractograph of the wrought sample shows a distinct morphology, with MC-type carbides inside the larger dimples. At the wrought sample shows a distinct morphology, with MC-type carbides inside the larger dimples. At

wrought sample shows a distinct morphology, with MC-type carbides inside the larger dimples. At same time, the second phase MC-type carbides are torn, as shown in Figure 17b. It is evident that the same time, the second phase MC-type carbides are torn, as shown in Figure 17b. It is evident that

the same time, the second phase MC-type carbides are torn, as shown in Figure 17b. It is evident that the MC-type carbides are primarily responsible for making the fracture process easier by providing the MC-type carbides are primarily responsible for making the fracture process easier by providing

the MC-type carbides are primarily responsible for making the fracture process easier by providing favorable sites for excessive microvoid initiation, and the growth of macroscopic cracks.
favorable sites for excessive microvoid initiation, and the growth of macroscopic cracks.
favorable sites for excessive microvoid initiation, and the growth of macroscopic cracks.

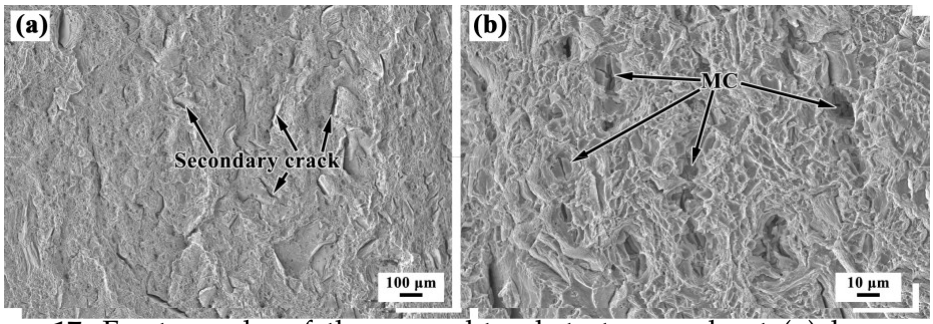

Figure 17. Fractographs of the wrought substrate sample at (**a**) low and (**b**) high magnifications.

Figure1717. Fractographs.ofofthethewroughtsubstratesubstratesampleatat(**a**()alow)lo wandand(**b**()**b**high)highmagnificationsmagnifications..

Figure 18 shows the fractographs of the LARed sample. A mixed fracture occurred in the
Figure 18 shows the fractographs of the LARed sample. A mixed fracture occurred in the
samples, which included the SZ and RZ, and the fractographs are quite different, as shown in Figure
samples, which included the SZ and RZ, and the fractographs are quite different, as shown in Figure 18a. Figure 18b shows the high-magnification SEM image of the SZ, which is similar to the wrought sample, where the fracture of the SZ contains a dimpled surface indicative of ductile failure, and there are particles inside the large dimples. The dimples and tear edges in the RZ fracture have a clear orientation, as shown in Figure 18c,d. Since the direction of the tensile stress at this time is almost perpendicular to the direction of the dendrite growth in the sample, the aligned dimples and tear edges also indicate that the microstructure of the LARed samples has a distinct orientation in the deposition direction. When the sample is stretched perpendicularly to the deposition direction, the dendritic structure is cut transversely, leaving a dimpled structure, with the dendrite center and dendrite dry areas as the torn edge. As the dendrite growth and dendrite column arrangement is regular, a rupture is left after the regular arrangement of the dimples.
regular, a rupture is left after the regular arrangement of the dimples.

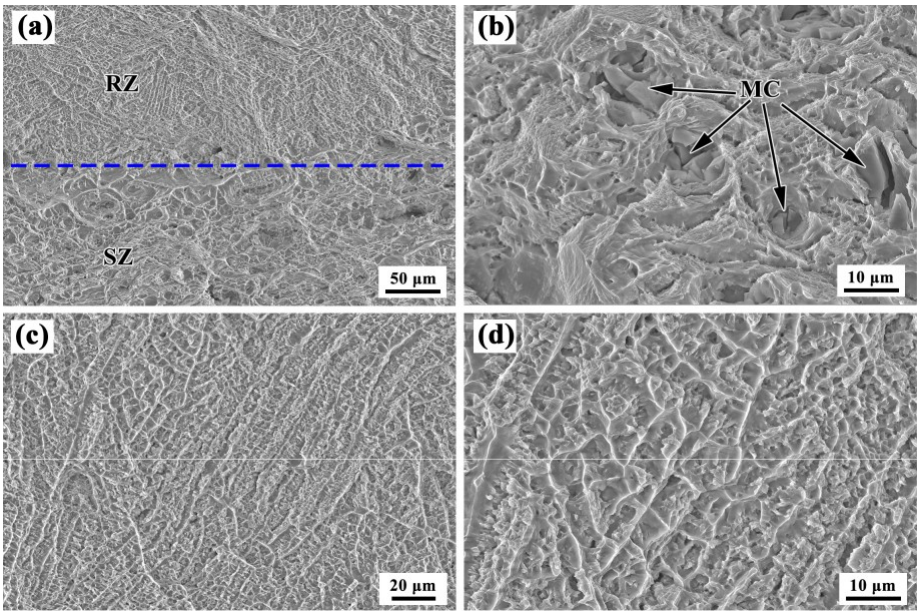

Figure 18. Fractograph of the LARed sample: (**a**) SZ+RZ, (**b**) SZ, and (**c**,**d**) RZ.

Figure 18. Fractograph of the LARed sample: (**a**) SZ+RZ, (**b**) SZ, and (**c**,**d**) RZ.

4. Conclusions

In this paper,, Inconelc l 625 alloy substratest with premade trapezoidal groove shaped defects were repaired using LAR. The microstructuresstr t s around the repairedir interfacet rf and the corresponding mechanical properties were investigated.. The conclusions are outlined below::

- The microstructurearound the the repaired repaired interface interface of of aLARed aLARed Inconel Inconel 625 625 alloy alloy can can bedivided bedivided into three into three zones: zonthes: SZ, the HAZ, SZ, HAZ, and RZ and The RZ SZ .The has SZ a typicalhas typical equiaxed equiaxed crystal struccryst t ure alstructure with a bimodalwith grain bimodal size grain distribution, size distribution, whileinthe while HAZ, in recrystallization the HAZ, recrystallization occursandleads occurs tosignificant andleads grain to growth significant. In grain the RZ, growth there . are In very theRZ, large there columnar arevery grains, large and columnar the size grains, of the and columns thesize increases ofthe with columns an increases with thenumber anincrease ofdeposited inthenumber layers. of deposited layers.
- The precipitatesin thein SZthemainlySZmaiconsistly consistoflarge (approximatelyoflarge(approxi10m)ately and small10μm)(approximatelyandsmall 0(approximately.5m)block-shaped0.5μm)MCblock-type-shapedcarbiesMC(M-typeisNbcarbiand esTi)(MandisirregularlyNbandTi)shapednd irregularlyflocculent Lavesshapedphaseflocculent.IntheLavesHAZ,phasethere. areInthestillHAZ,manytherelargeareblockstill-shapedmany largeMC-typeblockcarbides,-shaped butMCsom-type precipitatescarbides,butdissolveome precipitatesintheoriginaldissolvegrainboundariesintheoriginal.For thegrainRZ,boundariessomeLaves.ForandthefewRZ,MCsome-typ carbidesLavesandare precipitatedfewMC-

typealongcarbidestheepitaxialareprecipitatedgrowthdendriticalongboundartheepitaxial

es. growth dendritic

Theboundamicrostructureies. between two adjacent deposited tracks presented an overlapping transition

•

zoneThemicrostructure(OTZ),whichthebetweendendritictwostructureadjacentcoarsene

d,depositedandtracksmorepresentedLavesphasen ovprerlappingcipitated

comparedtransition tozonein the(OTZ),layer whichinteriorthe.Thedenwidthriticof

structuretheOTZ wascoarsened,approximatelyandmore0.15

Lavesmm.Thephaselowerprecip GRintatedhe

OTZcomparedledtotoaninincreasethelayerin interiordendrite.Thearmwidthspacingof

theandOTZthe formwasationpproximatelyoftheLaves0.15phasemm.. The lower TheG·R

inVickerstheOTZhardnessledtoanandincreaseindentationdendritemodulusarm

spacingfromtheandSZtheto formationtheRZalongofthethe Lavesdepositionphase.

- dirThection Vickers were hardness notnotably and diindentationerentthe modulus LARed samples, fromthe and SZ were tothe approximately RZalongthe 240 deposition 20HV. The direction microhardness werenot notably ofthematrix different phase in the inthe LARed RZ(approximately samples,andwere 5.1GPa) approximately wasslightly 240 higher ±20 than HV. that The of microhardness theSZ(approximately ofthematrix 4.8GPa), phase while inthe the RZ microha (app rdness oximately generally 5.1GPa) achieved was slightly alower value higher (approximately thanthatofthe 4. SZ 6GPa) (approximately intheHAZ. 4 In .8 particular, GPa),while the the microhardness microhardness of the generally matrix achieved phasein the alower OTZ value was(approximately4.7 4 GPa, .6GPa) which in the was HAZ slightly .In lower particular, than that the of microhardness layerinterior of in the RZ matrix (approximately phaseinthe 5.1 OTZ GPa) was .The approximately fluctuationof the 4.7 microhardness GPa,whichwas of the slightly matrix lower phase than around that the of repaired layerinterior interface the was RZ mainly(approximately causedb the 5.1 segregation GPa).Thefluctuation oftheNb and ofthe Mo microhardness alloyingelements ofthe.

matrix phase around the repaired interface was mainly caused by the segregation of the Nb and

The yield strength and elastic modulus of the LARed samples were higher than those of the

Mo alloying elements.

wrought sample. The tensile strength and ductility of the LARed samples were similar to those of

- The yield strength and elastic modulus of the LARed samples were higher than those of the the wrought sample. Both the SZ and RZ presented a dimple fracture surface, and a large number wrought sample. The tensile strength and ductility of the LARed samples were similar to those of secondary cracks could be found in the SZ. The dimples and tear edges had a clear orientation of the wrought sample. Both the SZ and RZ presented a dimple fracture surface, and a large number of secondary cracks could be found in the SZ. The dimples and tear edges had a clear

in the RZ. The comprehensive tensile properties of the LARed Inconel 625 alloy are equivalent to those of the wrought alloy.

Author Contributions: Y.W., Q.X. and G.L. conceived and designed the experiments; Y.W. and L.Y. performed the experiments; Y.W., Q.X. and G.L. analyzed the data; R.L. and W.W. contributed analysis tools; Y.W. wrote the paper. All authors have read and agreed to the published version of the manuscript.

Funding: This research was funded by the National Key Technologies R & D Program, China, grant number 2016YFB0700404.

Conflicts of Interest: The authors declare no conflict of interest.

References

1. Gao, Y.; Ding, Y.; Chen, J.; Xu, J.; Ma, Y.; Wang, X. E ect of Twin Boundaries on the Microstructure and Mechanical Properties of Inconel 625 Alloy. Mater. Sci. Eng. A **2019**, 767, 138361. [CrossRef]
2. Salarian, M.; Asgari, H.; Vlasea, M. Pore Space Characteristics and Corresponding E ect on Tensile Properties of Inconel 625 Fabricated Via Laser Powder Bed Fusion. Mater. Sci. Eng. A **2020**, 769, 138525. [CrossRef]
3. Hu, Y.L.; Lin, X.; Yu, X.B.; Xu, J.J.; Lei, M.; Huang, W.D. E ect of Ti Addition on Cracking and Microhardness of Inconel 625 During the Laser Solid Forming Processing. J. Alloys Compd. **2017**, 711, 267–277. [CrossRef]
4. Mostafaei, A.; Behnamian, Y.; Krimer, Y.L.; Stevens, E.L.; Luo, J.L.; Chmielus, M. E ect of Solutionizing and Aging on the Microstructure and Mechanical Properties of Powder Bed Binder Jet Printed Nickel-Based Superalloy 625. Mater. Des. **2016**, 111, 482–491. [CrossRef]
5. Nguejio, J.; Szmytka, F.; Hallais, S.; Tanguy, A.; Nardone, S.; Martinez, M.G. Comparison of Microstructure Features and Mechanical Properties for Additive Manufactured and Wrought Nickel Alloys 625. Mater. Sci. Eng. A **2019**, 764, 138214. [CrossRef]
6. Kumar, A.; Rajkumar, K.V.; Jayakumar, T.; Raj, B.; Mishra, B. Ultrasonic Measurements for in-Service Assessment of Wrought Inconel 625 Cracker Tubes of Heavy Water Plants. J. Nucl. Mater. **2006**, 350, 284–292. [CrossRef]
7. Debroy, T.; Wei, H.L.; Zuback, J.S.; Mukherjee, T.; Elmer, J.W.; Milewski, J.O.; Beese, A.M.; Wilson-Heid, A.; De, A.; Zhang, W. Additive Manufacturing of Metallic Components-Process, Structure and Properties. Prog. Mater. Sci. **2018**, 92, 112–224. [CrossRef]
8. Herzog, D.; Seyda, V.; Wycisk, E.; Emmelmann, C. Additive Manufacturing of Metals. Acta Mater. **2016**, 117, 371–392. [CrossRef]
9. Sui, S.; Chen, J.; Zhang, R.; Ming, X.; Liu, F.; Lin, X. The Tensile Deformation Behavior of Laser Repaired Inconel 718 with a Non-Uniform Microstructure. Mater. Sci. Eng. A **2017**, 688, 480–487. [CrossRef]
10. Onuike, B.; Bandyopadhyay, A. Additive Manufacturing in Repair: Influence of Processing Parameters on Properties of Inconel 718. Mater. Lett. **2019**, 252, 256–259. [CrossRef]
11. Zhao, Z.; Chen, J.; Tan, H.; Lin, X.; Huang, W. Evolution of Plastic Deformation and its E ect on Mechanical Properties of Laser Additive Repaired Ti64Eli Titanium Alloy. Opt. Laser Technol. **2017**, 92, 36–43. [CrossRef]

12. Balasubramanian, V.; Ravisankar, V.; Reddy, G.M. E ect of Pulsed Current and Post Weld Aging Treatment on Tensile Properties of Argon Arc Welded High Strength Aluminium Alloy. Mater. Sci. Eng. A **2007**, 459, 19–34. [CrossRef]
13. Liu, H.; Wang, X.; Ji, H. Fabrication of Lotus-Leaf-Like Superhydrophobic Surfaces Via Ni-Based Nano-Composite Electro-Brush Plating. Appl. Surf. Sci. **2014**, 288, 341–348. [CrossRef]
14. Pawlowski, L. Finely Grained Nanometric and Submicrometric Coatings by Thermal Spraying: A Review. Surf. Coat. Technol. **2008**, 202, 4318–4328. [CrossRef]
15. Saboori, A.; Aversa, A.; Marchese, G.; Biamino, S.; Lombardi, M.; Fino, P. Application of Directed Energy Deposition-Based Additive Manufacturing in Repair. Appl. Sci. **2019**, 9, 3316. [CrossRef]
16. Lin, X.; Cao, Y.; Wu, X.; Yang, H.; Chen, J.; Huang, W. Microstructure and Mechanical Properties of Laser Forming Repaired 17-4Ph Stainless Steel. Mater. Sci. Eng. A **2012**, 553, 80–88. [CrossRef]
17. Sun, S.D.; Liu, Q.; Brandt, M.; Luzin, V.; Cottam, R.; Janardhana, M.; Clark, G. E ect of Laser Clad Repair on the Fatigue Behaviour of Ultra-High Strength Aisi 4340 Steel. Mater. Sci. Eng. A **2014**, 606, 46–57. [CrossRef]
18. Liu, Q.; Wang, Y.; Zheng, H.; Tang, K.; Li, H.; Gong, S. Tc17 Titanium Alloy Laser Melting Deposition Repair Process and Properties. Opt. Laser. Technol. **2016**, 82, 1–9. [CrossRef]
19. Puppala, G.; Moitra, A.; Sathyanarayanan, S.; Kaul, R.; Sasikala, G.; Prasad, R.C.; Kukreja, L.M. Evaluation of Fracture Toughness and Impact Toughness of Laser Rapid Manufactured Inconel-625 Structures and their Co-Relation. Mater. Des. **2014**, 59, 509–515. [CrossRef]
20. Li, C.; White, R.; Fang, X.Y.; Weaver, M.; Guo, Y.B. Microstructure Evolution Characteristics of Inconel 625 Alloy from Selective Laser Melting to Heat Treatment. Mater. Sci. Eng. A **2017**, 705, 20–31. [CrossRef]
21. Wang, P.; Zhang, B.; Tan, C.C.; Raghavan, S.; Lim, Y.; Sun, C.; Wei, J.; Chi, D. Microstructural Characteristics and Mechanical Properties of Carbon Nanotube Reinforced Inconel 625 Parts Fabricated by Selective Laser Melting. Mater. Des. **2016**, 112, 290–299. [CrossRef]
22. Kreitcberg, A.; Brailovski, V.; Turenne, S. E ect of Heat Treatment and Hot Isostatic Pressing on the Microstructure and Mechanical Properties of Inconel 625 Alloy Processed by Laser Powder Bed Fusion. Mater. Sci. Eng. A **2017**, 689, 1–10. [CrossRef]
23. Dinda, G.P.; Dasgupta, A.K.; Mazumder, J. Laser Aided Direct Metal Deposition of Inconel 625 Superalloy: Microstructural Evolution and Thermal Stability. Mater. Sci. Eng. A **2009**, 509, 98–104. [CrossRef]
24. Rombouts, M.; Maes, G.; Mertens, M.; Hendrix, W. Laser Metal Deposition of Inconel 625: Microstructure and Mechanical Properties. J. Laser Appl. **2012**, 24, 2575–2581. [CrossRef]
25. Rivera, O.G.; Allison, P.G.; Jordon, J.B.; Rodriguez, O.L.; Brewer, L.N.; McClelland, Z.; Whittington, W.R.; Francis, D.; Su, J.; Martens, R.L. Microstructures and Mechanical Behavior of Inconel 625 Fabricated by Solid-State Additive Manufacturing. Mater. Sci. Eng. A **2017**, 694, 1–9. [CrossRef]

26. Tian, Y.; Ouyang, B.; Gontcharov, A.; Gauvin, R.; Lowden, P.; Brochu, M. Microstructure Evolution of Inconel 625 with 0.4 Wt% Boron Modification During Gas Tungsten Arc Deposition. J. Alloys Compd. **2017**, 694, 429–438. [CrossRef]
27. Xu, F.J.; Lv, Y.H.; Xu, B.S.; Liu, Y.X.; Shu, F.Y.; He, P. E ect of Deposition Strategy on the Microstructure and Mechanical Properties of Inconel 625 Superalloy Fabricated by Pulsed Plasma Arc Deposition. Mater. Des. **2013**, 45, 446–455. [CrossRef]
28. Xu, X.; Mi, G.; Chen, L.; Xiong, L.; Jiang, P.; Shao, X.; Wang, C. Research on Microstructures and Properties of Inconel 625 Coatings Obtained by Laser Cladding with Wire. J. Alloys Compd. **2017**, 715, 362–373. [CrossRef]
29. Hu, X.; Xue, Z.; Zhao, G.; Yun, J.; Shi, D.; Yang, X. Laser Welding of a Selective Laser Melted Ni-Base Superalloy: Microstructure and High Temperature Mechanical Property. Mater. Sci. Eng. A **2019**, 745, 335–345. [CrossRef]
30. Xu, X.; Lin, X.; Yang, M.; Chen, J.; Huang, W. Microstructure Evolution in Laser Solid Forming of Ti-50Wt% Ni Alloy. J. Alloys Compd. **2009**, 480, 782–787. [CrossRef]
31. Wang, J.F.; Sun, Q.J.; Wang, H.; Liu, J.P.; Feng, J.C. E ect of Location on Microstructure and Mechanical Properties of Additive Layer Manufactured Inconel 625 Using Gas Tungsten Arc Welding. Mater. Sci. Eng. A **2016**, 676, 395–405. [CrossRef]
32. Kurz, W.; Fisher, D.J. Dendrite Growth at the Limit of Stability: Tip Radius and Spacing. Acta Metall. **1981**, 29, 11–20. [CrossRef]
33. Lin, X.; Yue, T.M.; Yang, H.O.; Huang, W.D. Laser Rapid Forming of Ss316L/Rene88Dt Graded Material. Mater. Sci. Eng. A **2005**, 391, 325–336. [CrossRef]
34. Collins, P.C.; Brice, D.A.; Samimi, P.; Ghamarian, I.; Fraser, H.L. Microstructural Control of Additively Manufactured Metallic Materials. Annu. Rev. Mater. Res. **2016**, 46, 63–91. [CrossRef]
35. Ram, G.D.J.; Reddy, A.V.; Rao, K.P.; Reddy, G.M. Improvement in Stress Rupture Properties of Inconel 718 Gas Tungsten Arc Welds Using Current Pulsing. J. Mater. Sci. **2005**, 40, 1497–1500. [CrossRef]
36. Oliver, W.C.; Pharr, G.M. An Improved Technique for Determining Hardness and Elastic Modulus Using Load and Displacement Sensing Indentation Experiments. J. Mater. Res. **1992**, 7, 1564–1583. [CrossRef]
37. Yu, L.; Wang, W.; Su, B.; Wang, Z.; Qu, F.; Wu, H.; Pu, Z.; Meng, X.; Wang, Q.; Wang, J.; et al. Characterizations on the Microstructure and Micro-Mechanics of Cast be-Al-0.4Sc-0.4Zr Alloy Prepared by Vacuum Induction Melting. Mater. Sci. Eng. A **2019**, 744, 512–524. [CrossRef]